



HHS Public Access

Author manuscript

Int J Comput Assist Radiol Surg. Author manuscript; available in PMC 2019 March 18.

Published in final edited form as:

Int J Comput Assist Radiol Surg. 2018 November ; 13(11): 1829–1841. doi:10.1007/s11548-018-1839-y.

Development of a shoulder-mounted robot for MRI-guided needle placement: phantom study

Reza Monfaredi¹, Iulian Iordachita², Emmanuel Wilson¹, Raymond Sze³, Karun Sharma¹, Axel Krieger⁴, Stanley Fricke⁵, and Kevin Cleary¹

¹Sheikh Zayed Institute for Pediatric Surgical Innovation, Children's National Health System, Washington, DC, USA

²Laboratory for Computational Sensing and Robotics (LCSR), Johns Hopkins University, Baltimore, MD, USA

³Department of Radiology, Children's Hospital of Philadelphia, Philadelphia, PA, USA

⁴Department of Mechanical Engineering, University of Maryland, College Park, MD, USA

⁵Department of Diagnostic Imaging and Radiology, Children's National Health System, Washington, DC, USA

Abstract

Purpose—This paper presents new quantitative data on a signal-to-noise ratio (SNR) study, distortion study, and targeting accuracy phantom study for our patient-mounted robot (called Arthrobot). Arthrobot was developed as an MRI-guided needle placement device for diagnostic and interventional procedures such as arthrography.

Methods—We present the robot design and inverse kinematics. Quantitative assessment results for SNR and distortion study are also reported. A respiratory motion study was conducted to evaluate the shoulder mounting method. A phantom study was conducted to investigate end-to-end targeting accuracy. Combined error considering targeting accuracy, respiratory motion, and structure deformation is also reported.

Results—The SNR study showed that the SNR changes only 2% when the unpowered robot was placed on top of a standard water phantom. The distortion study showed that the maximum distortion from the ground truth was 2.57%. The average error associated with respiratory motion was 1.32 mm with standard deviation of 1.38 mm. Results of gel phantom targeting studies indicate average needle placement error of 1.64 mm, with a standard deviation of 0.90 mm.

Conclusions—Noise and distortion of the MR images were not significant, and image quality in the presence of the robot was satisfactory for MRI-guided targeting. Combined average total error, adding mounting stability errors and structure deformation errors to targeting error, is estimated to

Correspondence to: Reza Monfaredi.

Conflict of interest There is no conflict of interest.

Ethical approval All procedures performed in studies involving human participants were IRB-approved and were in accordance with the ethical standards of the institutional and/or national research committee.

Informed consent Informed consent was obtained from all individual participants included in the study.

be 3.4 mm with a standard deviation of 1.65 mm. In clinical practice, needle placement accuracy under 5 mm is considered sufficient for successful joint injection during shoulder arthrography. Therefore, for the intended clinical procedure, these results indicate that Arthrobot has sufficient positioning accuracy.

Keywords

MRI-compatible robot; Percutaneous procedures; Patient-mounted

Introduction

Arthrography, biopsy, facet joint injection, and other percutaneous interventions are typically performed using X-ray-based imaging guidance. Conventional image-guided interventions require the interventional radiologist to manually position the needle tip in the desired position seen on 2-D or 3-D images [1–3]. These manipulations often require multiple passes to reach the target, which prolong procedure time and exposes both patient and radiologist to undesired ionizing radiation associated with computed tomography (CT) or fluoroscopy guidance [4, 5]. Different groups have focused on manual MRI-guided procedures to deal with these drawbacks. Wu et al. [6] successfully performed MRI-guided manual biopsy of musculoskeletal lesions on 23 patients. Fritz et al. [7] performed freehand real-time MRI-guided lumbar spinal injection procedures on 37 patients with 89% success rate for facet joint injections.

MRI-compatible robots can be an enabling technology for MRI-guided, radiation-free procedures. In pediatric populations, where minimizing the use of ionizing radiation is especially important, this may be particularly important.

Arthrography is the evaluation of joint conditions using imaging modalities such as CT and MRI. It requires injection of contrast material within the joint to distend the joint capsule and better visualize the internal structures. Magnetic resonance (MR) arthrography is the modality of choice for evaluation of suspected derangements of internal joint structures such as the articular cartilage, labrum, ligaments and tendons because it has higher soft tissue contrast than other modalities. In current practice, MR arthrography requires two separate stages: an intra-articular contrast injection guided by fluoroscopy, followed by acquisition of diagnostic MRI images. This two-stage conventional method is suboptimal because the patient has to move from the fluoroscopy procedure room to the MRI room and may have to wait before the MRI room becomes available. During this time, the intra-articular contrast can begin to diffuse out of the joint space. In addition, needle insertion may require multiple passes before reaching the target area, which could result in increased procedure time, prolonged sedation time in younger patients, increased patient anxiety, and radiation exposure from fluoroscopic imaging. The procedure may also result in increased cost due to the use of two imaging modalities and suboptimal use of valuable hospital equipment, space, and time.

Being able to perform a complete MR arthrography procedure solely in the MRI scanner could address some of these issues. However, access to the patient in a closed-bore MRI scanner is challenging and multiple needle passes are not ideal. Given these constraints, we

believe a small, patient-mounted robot which could facilitate accurate needle placement under MRI guidance is an ideal solution for single-step arthrography procedures. Based on clinical feedback from three senior radiologists who routinely perform fluoroscopy-guided joint injections, the access window for reaching the shoulder joint space is at least 5 mm, even in patients as young as 10 years of age. Therefore, in clinical practice, needle placement accuracy of 5 mm would be sufficient. Other needle-based procedures under MRI such as prostate biopsy have similar requirements [8].

The high magnetic field present in the MRI environment, interaction with radiofrequency (RF) signals, and switching gradients are major challenges in developing MRI-compatible equipment. The mechanical linkages, actuators, encoders, and sensors that are key elements of any robotic system need to be selected carefully to minimize or avoid noises, artifacts, and distortions to MR images.

A few research groups have reported related work in the field of patient-mounted robots for percutaneous interventions. Walsh et al. [9] developed a patient-mounted robot called Robopsy. The robot is attached to the patient via an adhesive pad and optional strap points, allowing the device to move passively with patient motion. An MRI coil-mounted robotic positioner for cryoablation was developed in [10]. This 2-degrees of freedom (DOF), cable-driven robot had a multi-probe head for decreasing the ablation time. Maurin et al. [11] developed a patient-mounted robot using a 5-DOF parallel structure with a hemispherical workspace, particularly well-suited to CT-based interventional procedures. The whole robot can be sterilized, and its mechanical positioning error was less than 5 mm [12]. Bricault et al. [13] developed a light (1 kg) and compact (15 by 23 cm) robot with 5 DOFs to perform abdominal and thoracic punctures under CT or MRI guidance for diagnostic or therapeutic purposes. Song et al. developed a 2-DOF MRI-compatible double-ring RCM mechanism for MRI-guided liver interventions. This device was a passive mechanism that was manually operated [14].

A table-mounted MRI-compatible robot also gained some interest in the research community [15, 16]. However, repeated movement of the patient in and out of the scanner between scanning and needle placement steps could make this approach time-consuming. For procedures that are performed under local anesthesia, there is an increased chance that the patient moves unintentionally during the procedure resulting in robot to patient registration error and probably missing the selected target. Patient motion while the needle inserted into the patient's body also puts the patient in risk of injury. While the introduction of this paper focuses on patient-mounted MRI-compatible robotics systems, a more complete overview of MRI-compatible robotic system can be found in [17, 18].

We have developed a novel MRI-compatible, patient-mounted robot for diagnostic and interventional percutaneous procedures which should enable accurate needle placement in a single pass under MRI guidance. The arthrography procedure is considered as the initial application for this device. The robot provides a stable guide for the needle insertion which will be done manually by the physician. Manually driven needle insertion was considered in this prototype to reduce the risk of needle manipulation and to reduce regulatory drawbacks. For the shoulder arthrography procedure, manual needle drive is sufficient since the

radiologist can push the needle in until the bone is hit, and there are only a few critical structures nearby to be concerned with.

By automated registration of MR images and patient coordinates, the number of needle passes and procedure time could be reduced. The proposed workflow for robotic-assisted arthrography, design and fabrication of the robot, mounting method and mounting accuracy, as well as results of qualitative SNR and distortion study, have been published before [19–21].

In this paper, we derived the inverse kinematic of our robot, present the implementation of motion control and registration scheme, and conducted targeting experiment to investigate the overall accuracy of the system. Quantitative results for SNR and distortion are also reported.

The rest of the paper is organized as follows. Section two describes inverse kinematics and registration method. In section three, the experimental setup and results for quantitative MRI compatibility study and distortion study have been discussed. Next, a gel phantom accuracy study is reported. Section four discusses and reports the overall system accuracy. Conclusions are given in section five.

Methods

Figure 1 shows a CAD model and prototype of the current robot. The parts were all 3D printed by a rapid prototyping machine (Objet 500, Stratasys) using VeroWhite Material. This robot has 4 DOFs: 2 DOFs for needle translation (θ_3 and d_1) and 2 DOFs for needle orientation adjustment (θ_1 and θ_2).

As shown in the CAD model in Fig. 1a, a four-link parallel mechanism with a spherical joint is used, yielding 2 rotations about the spherical joint. As shown in Fig. 1b, motor 1 rotates the needle guide about the x -axis (θ_1) and motor 2 rotates it about the y -axis (θ_2).

Motor 3 provides translational motion along the link 4 through a timing belt and a pair of pulleys. The four-link parallel mechanism base, link 4, slides through the robot base to add the third DOFs, i.e., d_1 . Motor 4 is embedded in the robot to provide the 4th DOF, i.e., θ_3 . This motor rotates the entire four-link parallel mechanism using a pair of spur gears. The combination of the translational motion (d_1) with the rotation of the robot base (θ_3) provides maneuverability in xy plane. MRI-compatible piezo-motors (Piezo LEGS® Uppsala, Sweden) and MRI-compatible encoders: E8P OEM Optical Kit Encoder, 512 CPR, 1/8 bore, differential, hole in (US digital, Vancouver, Washington, USA) were used for joint actuation and measurement.

A ceramic ball bearing (ID = 90 mm, Boca Bearing Inc., FL, USA) was used for the base rotation to provide frictionless base rotation. Two plastic linear bearings (Designatronics Inc., NY, USA) were used for the linear DOF. The robot ranges of motion are ± 35 mm (θ_3 and d_1 provide xy positioning) and $\pm 45^\circ$ (θ_1 and θ_2) for the translational and rotational workspace. In the current configuration of the robot, needle insertion is done manually through a needle guide. Automatic needle drive system is considered for the future version

of the robot. It was excluded from current version because of the possible regulatory drawbacks. Our target population is patients aged 10 and older. We believe that the current design can fit properly to the shoulder of patient in these patients. It is also possible to design smaller mounting adaptors to attach the same robot to smaller patients. Based on [22, 23], average shoulder length for American adult male is 169 mm and for adult female is 131 mm. Based on [24], boys, ages 10 and older, have grown up to 72% of their adulthood size and girls, ages 10 and older, have grown up to 82% of their adulthood size. Therefore, the estimated average shoulder length for our study group is 121.6 mm and 107.5 mm for boys and girls, respectively. The maximum diameter of the adaptor for mounting of the robot is 100 mm and could be customized to be smaller. Therefore, the suggested size for the mounting adaptor is reasonable for the specified age group.

Inverse kinematics

To position and orient the needle guide based on the entry and target points, selected by physician, the inverse kinematics of the robot is required. In this section, inverse kinematics of the robot has been derived.

Four coordinate frames are shown in Fig. 2a, b as follows: (1) robot coordinate frame, r , located in the center of the robot base, (2) the Center of Motion (CM) coordinate frame, CM , which moves with CM point, (3) rotated CM coordinate frame CM' , and (4) scanner coordinate frame s . As shown in Fig. 2a, rotated CM coordinate frame has an offset angle, i.e., $\alpha = 19.5$, with respect to CM coordinate frame about y -axis. CM point, i.e., the origin of CM coordinate frame, moves in xy plane of r where $r_z = 0$. θ_1 , θ_2 , θ_3 , and d_1 are the robot's joint space coordinates.

To control the robot to reach the desired position and orientation, the transformation matrices, ${}_{CM}^r T$ and ${}^s_r T$ are required, where ${}_{CM}^r T$ is the transformation from CM coordinate frame to robot coordinate frame, and ${}^s_r T$ is the transformation matrix from the robot coordinate frame to the scanner coordinate frame. ${}^s_r T$ matrix is derived from the MRI images using segmentation information for three perpendicular tube fiducials embedded in the base of the robot as described in section II-part D.

In Fig. 2b, point E and T represent the entry and target points which are selected on MRI image by the physician. Using these two points, the desired direction of the needle is calculated which is along the vector ${}^s r_{E,T}$ as shown in Fig. 2a, b. The following equations were used to map ${}^s r_{E,T}$ from the scanner coordinate system to the CM coordinate frame:

$${}^s r_{E,T} = {}^s r_T - {}^s r_E, \quad {}_{CM}^r r_{E,T} = {}_{CM}^r T {}^s r_{E,T} \quad (1)$$

$${}_{CM}^r T = {}_{CM}^r T^{-1} {}^s_r T \quad (2)$$

where ${}^r r_E$ and ${}^r r_T$ are the coordinate vectors corresponding to entry point and target point in scanner coordinate frame.

As shown in Fig. 2a, line L is along the vector ${}^{CM} r_{E, T}$ which intersects xy plane of the robot coordinate frame at point N , i.e., ${}^r z = 0 = 0$. The equation for line L is:

$$\frac{{}^r x - {}^r x_T}{a} = \frac{{}^r y - {}^r y_T}{b} = \frac{{}^r z - {}^r z_T}{c} \quad (3)$$

where a , b , and c are given by ${}^r r_{E, T} = {}^r r_T - {}^r r_E = ai + bj + ck$. ${}^r r_T = [{}^r x_T \ {}^r y_T \ {}^r z_T]$ is the coordinate vector of the target point in robot coordinate frame obtained as:

$${}^r r_T = {}^r T^s r_T - {}^r T^s r_o \quad (4)$$

where ${}^s r_o$ is the coordinate vector of the robot origin in the scanner coordinate frame which is estimated based on the center point coordinates of fiducials embedded in the robot base. Coordinates of center point of fiducials are obtained from segmentation information as described in section II-part D. The target point should be far below the entry point under the skin (< 10 mm). Therefore, we can assume that $c = |{}^r z_T - {}^r z_E| \gg 0$. If $a = 0$ or $b = 0$ then Eq. (3) could be simplified to:

$$\frac{{}^r y - {}^r y_T}{b} = \frac{{}^r z - {}^r z_T}{c} \quad (\text{if } a = 0) \quad (5)$$

$$\frac{{}^r x - {}^r x_T}{a} = \frac{{}^r z - {}^r z_T}{c} \quad (\text{if } b = 0) \quad (6)$$

To align the needle along the desired trajectory, first the CM point should move to the point N (see Fig. 2a). The x and y coordinates of this point in the robot coordinate system, i.e., ${}^r x_N$, ${}^r y_N$, could be obtained using (3) as follows:

$${}^r x_N = {}^r x_T - \frac{a}{c} {}^r z_T \quad (7)$$

$${}^r y_N = {}^r y_T - \frac{b}{c} {}^r z_T \quad (8)$$

Combining the translational motion of the robot, d_1 , and rotation of the robot base, θ_3 , robot CM point could be moved to $[{}^r x_N \ {}^r y_N]$. Providing ${}^r x$ and ${}^r y$, d_1 and θ_3 are obtained as:

$$d_1 = \sqrt{{}^r x_N^2 + {}^r y_N^2} \quad (9)$$

$$\theta_3 = a \tan({}^r y_N / {}^r x_N), \quad \theta_3 \in [-\pi / 2, +\pi / 2] \quad (10)$$

Given d_1 and θ_3 , $CM' T$ could be obtained by rotating robot coordinate frame with the amount of θ_3 about z -axis and transforming with the amount of d_1 in xy plane. The needle guide should be aligned along vector ${}^{CM'} r_{E,T}$. To find the rotation angle between the vector ${}^{CM'} r_{E,T}$ and the x and y axes of CM coordinate frame, ${}^{CM'} r_{E,T}$ is projected into the yz plane of the CM' coordinate system as shown in Fig. 3.

As shown in Fig. 3, θ_1 is the rotation of needle guide (${}^{CM'} r_{E,T}$), initially aligned with the z -axis, about the x -axis of CM' , and θ_2 is the rotation of ${}^{CM'} r_{E,T}$ about y -axis of CM' . θ_1 and θ_2 are obtained as:

$$\theta_1 = A \cos \left(\frac{\left| z_{\text{Proj}_{zy}} \left({}^{CM'} r_{E,T} \right) \right|}{\left| \text{Proj}_{zy} \left({}^{CM'} r_{E,T} \right) \right|} \right) \quad (11)$$

$$\theta_2 = A \cos \left(\frac{\left| \text{Proj}_{zy} \left({}^{CM'} r_{E,T} \right) \right|}{\left| {}^{CM'} r_{E,T} \right|} \right) \quad (12)$$

where $\text{Proj}_{zy}(V)$ represents projection of vector V in yz plane and $z_{\text{Proj}_{zy}}(V)$ represents z component of projection of vector V in yz plane. where

$$\left| {}^{CM'} r_{E,T} \right| = \sqrt{\left(x \left({}^{CM'} r_{E,T} \right) \right)^2 + \left(y \left({}^{CM'} r_{E,T} \right) \right)^2 + \left(z \left({}^{CM'} r_{E,T} \right) \right)^2},$$

and

$$\left| \text{Proj}_{zy} \left({}^{CM'} r_{E,T} \right) \right| = \sqrt{\left(y \left({}^{CM'} r_{E,T} \right) \right)^2 + \left(z \left({}^{CM'} r_{E,T} \right) \right)^2}.$$

Control system

The key components of the control system are shown in Fig. 4 as follows: (1) the robot; (2) control box A which is placed in the control room; (3) control box B which is located in the MRI room; and (4) the user interface and computer. All power and signal cables between the

scanner room and the control room are passed through the patch panel. To minimize RF noise introduced into the MR environment, fiber optic cables are used to transmit motion control signals.

Control box A provides AC/DC voltage conversion and a communication interface with a control laptop. One media convertor (EIS-x-Sx Series, B&B Electronics Inc., Ottawa, IL) is used in each control box to convert electrical signals to optical signals. Thus, it provides optical communication between two control boxes through the patch panel waveguide. There is a DC–DC convertor in the control box A to convert output of the AC/DC voltage convertor (24v) to 12v which is required for the media convertor. 24v is passed through the patch panel using filtered connectors from control box A to provide a power source for control box A. There is another DC–DC convertor in the control box B to convert 24v to 12v as an input for the media convertor. Control box B also includes four drivers for Piezo-motors (PDA 3.1, Uppsala, Sweden) and one 4-axis Galil motion controller (DMC4143, Rocklin, CA).

A MATLAB-based application running on the control computer provides the software backend for image registration, motion control, and trajectory planning.

Mounting method and different source of inaccuracies

The mounting method should be (1) time-efficient, meaning easy to put on and take off the patient, and (2) stable, to provide a stable base for robot operation and needle placement. Our proposed mounting method satisfies these primary criteria. We used a ring adaptor and embedded it in a shoulder brace as shown in Fig. 5 to satisfy these criteria.

There are two different possible sources for robot displacement: (1) general patient motion and respiratory motion and (2) change in the center of gravity of the robot caused by robot motion from one position to another position that could cause displacement of the robot's base mounted on the body, plus robot displacement during needle insertion. We conducted experiments to investigate the stability of the mount and the error associated with the mounting method and change in the center of gravity. The average relative mounting error associated with change in the center of gravity for five subjects was reported as 0.44 mm with standard deviation of 0.19 mm [21]. In this paper, we investigated the error associated with respiratory motion/patient motion in Section III-part B.

Registration method

Four tube fiducials (REF 121, Beekley Corp., Bristol, CT, USA) are placed at the base of the robot for registration as shown in Fig. 6a. The (a), (b), and (c) fiducials are orthogonal. Therefore, the central axes of these fiducials define the robot coordinate system. As shown in Fig. 6, the (a) and (d) fiducials are parallel. These two fiducials are used to define the coordinate of the origin of the robot frame attached to the center of the robot and aligned with fiducials (a), (b), and (c). The coordinate of the robot frame origin is calculated as the average of the center point coordinates of the fiducials (a), and (d).

The Line Marker Registration (LMR) module in 3D Slicer [25] was used to automatically segment the fiducials and extract the coordinate of the fiducials center point and central

axes. The operator must manually define the fiducials corresponding to the robot x , y , and z axes, by clicking on the fiducials in MR images close to the center of the fiducials as shown in Fig. 6b. The approximate center of the fiducials should be selected in a known order to determine the x , y , and z axes of the robot frame.

Experimental results

In this section, we present the results of our experimental studies, including (1) MRI compatibility and (2) phantom study accuracy.

MRI compatibility study

The goals of these experiments were: (1) to study the distortions caused by the robot and (2) to evaluate SNR of images of standard water phantom with and without the robot. Each of these goals was addressed as described next.

Study of distortions caused by the robot—Any distortion in the MR images especially within the field of interest could make it difficult for the radiologist to reach the target point. In this subsection, the distortion study results are presented.

Goal: To investigate the image distortion of a grating phantom in the presence of the robot.

Experiment setup: A custom-made grating phantom (VirtualScopics Inc.) was filled with water and two different sets of images were obtained: (1) MRI images of the phantom itself (serving as ground truth) and (2) MRI images of the grating phantom with the robot placed on top.

A 1.5 Tesla Siemens Aera scanner was used to acquire MR images using the following scanning parameters: T1-weighted image, spin echo (SE), 2D, flip angle (FA) = 90, repetition time (TR) = 505 ms, echo time (TE) = 16 ms.

The grating phantom is shown in Fig. 7a, and an MR image of the phantom from the 1.5 Tesla Siemens scanner is shown in Fig. 7b. The cross lines in the images will show any distortion caused by artifacts. As expected, the image in Fig. 7b, with absence of any metallic object, shows no distortion. In the next step, the distortions due to the robot were studied. The robot was placed on the top of the grating phantom, and new images were acquired.

Results: Fig. 8 shows an MRI image about 1 mm below the top surface of grating phantom while the robot is placed on top. As shown in Fig. 8a, there is no significant distortion or artifact in the MR image. The robot is mostly made of ABS which is a plastic, and no artifacts are expected from plastics. The motors are more than 2.5 cm away to not cause significant distortion in the target image area [20].

The geometric distortion is defined by the NEMA standard MS 2-2008 as the maximum percent difference between measured distances in an image and the corresponding ground truth dimensions. Image 8b shows four different areas (i.e., a1–h1, a2–h2, a3–h3, and a4–h4) considered for the geometric distortion study based on NEMA standard MS 2-2008. The

ground truth dimensions were obtained by measuring the distance between corresponding points in the MRI image acquired before placing the robot on top of the phantom. Table 1 shows the distortion study result for different areas. In areal (i.e., a1–h1), the max distortion is 2.57% which is the largest distortion. In the next section, the clinical image quality will be investigated while the robot is on top of the subject's shoulder.

SNR study in the presence of the robot—In the proposed workflow, after positioning the needle guide at the predefined position and orientation, the robot will be turned off and a new set of MR images will be acquired to confirm the accurate placement of the needle guide and then the needle is manually inserted to reach the joint space. Once the contrast agent is injected to the joint space, the robot will be removed from the patient's shoulder before acquiring diagnostic images. Qualitative results for shoulder image quality study in the presence of robot have been reported in [20]. As reported in our previous publication [20], we presented images to two of our radiologists and they confirmed that the image quality, while the robot is mounted on the shoulder, is good enough for targeting the joint space. Based on our proposed workflow [20], the robot will be removed from the patient's shoulder for taking diagnostic images and in this step a flex coil similar to the current standard clinical workflow will be used to acquire diagnostic images with high quality. In this subsection, we report quantitative image quality assessment results.

Goal: To investigate the MR image quality when the unpowered robot is placed on the shoulder.

Method: Two sets of MRI images were obtained with and without the robot, using the following imaging parameters with the built-in spine coil: (a) T1-weighted image, SE, 2D, FA = 150, TE = 9.1 ms, and TR = 500 ms and (b) T2-weighted image, SE, 2D, FA = 180, TE = 57 ms, and TR = 3300 ms. The MRI technologist who helped with the study has over 10 years of clinical scanning experience and selected these standard MRI shoulder imaging sequences for this study.

Results: A quantitative signal-to-noise (SNR) experiment based on NEMA Standards MS 1-2008 (R2014) 4th method, using a standard cylindrical water phantom showed that SNR changes only 2.3% for T1-weighted images and 1.3% for T2-weighted images when the robot is powered off and is placed on top of the water phantom.

Investigating the effect of respiratory motion in relative displacement of the robot

While the shoulder joint is a rigid structure and not generally subject to respiratory motion, a part of robot sits on the patient chest, which could be affected by respiratory motion. In this section, we investigated the effect of respiratory motion/patient motion for positioning error in 3 subjects.

Goal: The goal of this section is to investigate the effect of respiratory motion on 3 subjects during a simulated procedure.

Experiment setup: To track the position and orientation of the robot's needle guide, a rigid body was attached to the needle guide as shown in Fig. 9. This rigid body consisted of

8 active embedded markers. An optical tracker (Certus, NDI, Waterloo, ON, Canada) was used to track the rigid body. The manufacturer's stated accuracy is 0.1 mm. The optical tracker was placed 1.5 m away from the markers.

One individual marker, i.e., marker 9, was attached to the shoulder brace as a reference points to provide relative measurement of the robot with respect to subjects' shoulder.

Experiment workflow and data collection: The robot was snapped into the adaptor embedded in a shoulder brace as described in Section II-part C, as shown in Fig. 9. Each of the three subjects was instructed to stay in supine position for 20 min, while they were breathing normally. The optical tracker was used to measure and record (at 100 Hz) the position/orientation of the rigid body as well as positions of two reference markers attached to the subject's shoulder brace in order to measure displacement of the robot with respect to the shoulder during regular breathing.

Results: As shown in Table 2, the total average positional displacement of the robot is 0.84 mm with standard deviation of 0.74 mm. The total average rotational displacement of the robot is 0.34° with standard deviation of 0.46°. If the maximum depth of needle insertion is considered as 80 mm, this rotational displacement of the needle guide could result in 0.48 mm error with standard deviation of 0.64 mm. These errors are combined, and the final respiratory-related error is 1.32 mm with standard deviation of 1.38 mm as shown in Table 2.

Targeting accuracy study using a gel phantom

The robot targeting accuracy depends on different factors such as segmentation accuracy, registration accuracy, needle deformation, and errors inherent to the robot structure. A phantom study was done to investigate the total targeting accuracy caused by such factors.

Goal: Perform end-to-end targeting accuracy assessment using a gel phantom.

Experiment setup: To assess targeting accuracy in a laboratory environment a gel phantom was constructed as shown in Fig. 10. An inorganic ballistic gel (Clear Ballistics LLC., Fort Smith, AR) was set in a 7" diameter Pyrex dish. Plastic spheres of four different diameter sizes were used as targets (3.175 mm, 4, 4.75 mm, and 6.35 mm). The phantom consists of 3 layers with 15 mm, 30 mm, and 45 mm depth for first, second, and third layer, respectively. Each layer consists of the 4 different size spheres placed in a random location. The robot is snapped into the mounting adaptor as shown in Fig. 11. We created a ballistic gel phantom with 10% gelatin density. We used ballistic gel for making phantom since in the literature ballistic gel with water solutions containing 10–20% gelatin are widely used for muscle tissue simulants [26]. Therefore, we neglected the heterogeneous properties of human tissue which is especially significant for the patient skin. We assume that in the clinical workflow the radiologist will make an incision on the skin at the entry point to facilitate introduction of the needle.

MRI images of the gel phantom were acquired using the following imaging parameters: T1-weighted image, gradient recalled/inversion recovery (GR\IR), 3D, FA = 8, TE = 1.12 ms and TR = 2200 ms.

The tube fiducials in the MRI images were automatically segmented using the 3D Slicer/LMR module, and the robot coordinates vectors were estimated with respect to MRI image coordinate using tube fiducials (Beekley Corp., Bristol, CT, USA) as described in section II-part F. Each target point was reached from 3 different angles by selecting 3 random entry points at the surface of the gel phantom.

A MATLAB-based graphical user interface (GUI) was developed to enter entry and target points and to upload the segmentation information provided by 3DSlicer/LMR, written to a text file. The LMR module performs automatic segmentation and provides information about the center of the fiducials and a vector representing the axial direction of the fiducials. Figure 12 shows the MRI image of the gel phantom after automatic segmentation.

Entry and target points were selected from the preprocedural MR images. Entry points were chosen randomly at the surface of the gel phantom. Target points were identified as the center of the spherical fiducials. After computing the robot/MR image transformation matrix and performing kinematic calculations, the robot aligns the needle along the entry and target points. A 20-gauge bevel tip MRI-compatible needle (Chiba biopsy needle, Cook Inc., IN, USA) was used for targeting. The needle was manually inserted to reach the target. The depth of needle insertion was based on visual inspection of the needle tip relative to the target. To minimize the needle deformation, the needle was rotated periodically during the insertion. Depth control is not the focus of this paper since in conventional arthrography procedure the physician inserts the needle tip to touch and feel the bone. In order to be efficient with MRI time and also avoid the artifact of MRI-compatible needles, after each targeting we replaced the needle with a brass rod with the same diameter (0.9 mm). After withdrawing the needle, we replaced the brass rod through the same needle guide to make sure that the brass rod followed the previous path and by visual observation we confirmed accurate placement of the brass rod.

After repeating this for different targets and placing several brass rods, we acquired a set of MR images for calculating the targeting accuracy offline.

Results: Figure 13a shows the gel phantom after targeting study. MR images were acquired, and the distances between the center of each plastic sphere target with respect to the needle paths was estimated picking two points manually along the needle path and calculating the normal distance between the target point and line passing those selected points. All the plastics spheres are rigid, and the needle could not penetrate into these targets. Therefore, we report normal distance between needle axis and the center of the target as our accuracy measure. We were careful to precisely select these midpoints along the needle's center line. Then we carefully selected the center of the target in the MRI image and calculated the normal distance between this line and the center of the target.

Figure 13a shows the gel phantom with brass rods. Figure 13b shows the MR image of the gel phantom and one of the needle paths. The results of the targeting accuracy study summarized for each layer of fiducials are shown in Table 3. The average and standard deviation of phantom study errors is 1.64 mm and 0.90 mm.

Discussion

To estimate the total system error, the errors corresponding to (1) patient respiratory motion, (2) displacement of the needle guide during the operation due to change in center of gravity and radiologist interaction with the robot during the needle insertion step, and (3) accuracy of the phantom study accounted for robot accuracy and registration algorithm accuracy were investigated. Table 4 shows the errors for shoulder arthrography associated with each error source.

The mounting stability test showed that the average displacement of the robot during the procedure due to respiratory motion is $a_r = 1.32$ mm with standard deviation of $\sigma_r = 1.38$ mm. Average needle guide displacement during the procedure due to change in center of gravity, exertion of external forces during the needle insertion, and stability of the mounting mechanism was $a_m = 0.44$ mm with standard deviation of $\sigma_m = 0.19$ mm [21]. Phantom study shows that the average targeting accuracy of the robot in the laboratory is $a_p = 1.64$ mm with a standard deviation of $\sigma_p = 0.9$ mm. Since these errors are independent errors, the total estimated average error of the system would be sum of the errors, 3.4 mm, with the standard deviation of 1.65 mm ($\sqrt{\sigma_r^2 + \sigma_m^2 + \sigma_p^2}$). This result shows that the accuracy of our MRI-compatible robot is promising since for the most of the diagnostic and interventional procedures targeting accuracy better than 5 mm would be sufficient [16].

Conclusion

The use of advanced imaging for diagnosis and interventions continues to grow. MRI-guided interventions are an emerging field which has several advantages including better soft tissue visualization and no exposure to ionizing radiation. Several research groups have prototype robotic systems, but few clinical trials have been done. Our long-term goal is to develop MRI-compatible robotics for pediatric minimally invasive procedures. Toward this end, we have developed a novel workflow for shoulder arthrography to convert it from a two-stage procedure (X-ray-guided joint injection followed by MRI scanning) to a one-stage procedure that can be completely performed in the MRI room.

In this paper, the robot inverse kinematics was derived. Quantitative assessment results for SNR and distortion study were reported. Respiratory motion of 3 subjects was investigated to evaluate the mounting method. Finally, a phantom study was conducted to investigate end-to-end targeting accuracy.

MRI compatibility results showed no significant noise within the robot workspace when the unpowered robot was placed on the shoulder of a volunteer. Quantitative SNR study showed SNR variation of only 2.3% for T1-weighted images and 1.3% for T2-weighted images for the unpowered robot. Since in the proposed workflow the robot will be powered off before acquiring MRI images, these SNR study results are promising. Distortion study results showed maximum geometrical distortion of 2.57%.

The total estimated average error of the system was 3.4 mm with standard deviation of 1.65 mm. As noted in the introduction, needle placement accuracy of 5 mm is acceptable for this

procedure. Therefore, for the intended clinical procedure, these results indicate that the robot has sufficient positioning accuracy. Our next steps are to improve mounting method, to do an end-to-end accuracy study in the MRI suite, and pursue a clinical trial of shoulder arthrography at our pediatric hospital.

We are planning to add automatic needle drive mechanism to our robot in the future. By using automatic needle drive, we will be able to keep the patient in the MRI bore and use real-time MRI sequences to track the needle while inserting the needle.

Acknowledgments

Funding This work was partially supported by the National Institutes of Health (NIH) under Grants R01EB020003 and R21EB020700.

References

- Gopinathan A, Peh WCG (2011) Image-guided facet joint injection. *Biomed Imaging Interv J* 7(1):e4 [PubMed: 21655113]
- Srinivasan S, Peh WCG (2011) Imaging-guided biopsy in musculoskeletal infections. *Semin Musculoskelet Radiol* 15(5):561–568 [PubMed: 22081290]
- Hansford BG, Stacy GS (2012) Musculoskeletal aspiration procedures. *Semin Intervent Radiol* 29(4):270–285 [PubMed: 24293800]
- Magnusson A, Akerfeldt D (1991) CT-guided core biopsy using a new guidance device. *Acta Radiol* 32(1):83–85 [PubMed: 2012739]
- Onik G, Cosman ER, Wells T, Goldberg H, Moss AA, Costello P, Kane RA, Hoddick W, Demas B (1988) CT-guided aspirations for the body: comparison of hand guidance with stereotaxis. *Radiology* 166(2):389–394 [PubMed: 3275980]
- Wu HT, Chang CY, Chang H, Yen CC, Cheng H, Chen PC, Chiou HJ (2012) Magnetic resonance imaging guided biopsy of musculoskeletal lesions. *J Chin Med Assoc* 75(4):160–166 [PubMed: 22541144]
- Fritz J, Thomas C, Clasen S, Claussen CD, Lewin JS, Pereira PL (2009) Freehand real-time MRI-guided lumbar spinal injection procedures at 1.5 T: feasibility, accuracy, and safety. *Vasc Interv Radiol* 192(4):W161–W167
- Mozer PC, Partin AW, Stoianovici D (2009) Robotic image-guided needle interventions of the prostate. *Rev Urol* 11(1):7–15 [PubMed: 19390670]
- Walsh C, Hanumara NC, Slocum AH, Shepard JA, Gupta R (2008) A patient-mounted, telerobotic tool for CT-guided percutaneous interventions. *J Med Devices* 2(1):011007.1–011007.10
- Wu FY, Torabi M, Yamadak A, Golden A, Fischer GS, Tuncali K, Frey DD, Walsh C (2013) An MRI coil-mounted multiprobe robotic positioner for cryoablation. In: *Proceedings of the ASME International Design Engineering Technical Conferences & Computers and Information in Engineering Conference*, Portland, Oregon, USA, pp 1–9
- Maurin B, Bayle B, Piccin O, Gangloff J, de Mathelin M, Doignon C, Zanne P, Gangi A (2008) A patient-mounted robotic platform for CT-scan guided procedures. *IEEE Trans Biomed Eng* 55(10):2417–2425 [PubMed: 18838367]
- Hungr N, Fouard C, Robert A, Bricault I, Cinquin P (2011) Interventional radiology robot for CT and MRI-guided percutaneous interventions. *Med Image Comput Comput Assist Interv* 14(1):137–144 [PubMed: 22003610]
- Bricault I, Jouniaux E, Zemiti N, Fouard C, Taillant E, Dorandeu F, Cinquin P (2008) A light puncture robot for CT and MRI interventions. *IEEE Eng Med Biol Mag* 27(3):42–50
- Song SE, Tokuda J, Tuncali K, Yamada A, Torabi M, Hata N (2013) Design evaluation of a double ring RCM mechanism for robotic needle guidance in MRI-guided liver interventions. In: *IEEE/RSJ International Conference on Intelligent Robots and Systems (IROS)*, Tokyo, Japan, pp 4078–4083

15. Li G, Hao S, Cole GA, Shang W, Harrington K, Camilo A, Pilitsis JG, Fischer GS (2015) Robotic system for MRI-guided stereotactic neurosurgery. *IEEE Trans Biomed Eng* 62(4):1077–1088 [PubMed: 25376035]
16. Franco E, Brujic D, Rea M, Gedroyc WM, Ristic M (2015) Needle-guiding robot for laser ablation of liver tumors under MRI guidance. *IEEE ASME Trans Mechatron* PP(99):1–14
17. Elhawary H, Tse ZT, Hamed A, Rea M, Davies BL, Lamperth MU (2008) The case for MR-compatible robotics: a review of the state of the art. *Int J Med Robot* 4(2):105–113 [PubMed: 18481822]
18. Cleary K, Melzer A, Watson V, Kronreif G, Stoianovici D (2006) Interventional robotic systems: applications and technology state-of-the-art. *Minim Invasive Ther Allied Technol* 15(2):101–113 [PubMed: 16754193]
19. Monfaredi R, Sze R, Safdar N, Sharma K, Cleary K (2013) Patient mounted CT and MRI-compatible shoulder arthrography robot for needle guidance in pediatric interventional procedures. *The Hamlyn Symposium on Medical Robotics, London*, pp 117–118
20. Monfaredi R, Seifabadi R, Iordachita I, Sze R, Safdar NM, Sharma K, Fricke S, Krieger A, Cleary K (2014) A prototype body-mounted MRI-compatible robot for needle guidance in shoulder arthrography. In: *Proceedings of IEEE RAS & EMBS Int. Conf. Biomedical Robotics and Biomechatronics (BioRob)*, Sao Paulo, Brazil, pp 40–45
21. Monfaredi R, Wilson E, Sze R, Sharma K, Azizi B, Iordachita I, Cleary K (2015) Shoulder-mounted robot for MRI-guided arthrography: accuracy and mounting study. In: *International Conference of the IEEE Engineering in Medicine and Biology Society, Italy*, pp 3643–3646
22. Churchill E, McConville JE (1976) Sampling and data gathering strategies for future USAF Anthropometry Webb Associates, Inc. A/F Aerospace Medical Res 2-76, OHIO, AMRL-TR-74-102 1976
23. National Aeronautics and Space Administration (2018). <https://msis.jsc.nasa.gov/sections/section03.htm>
24. Rieser Patricia (2018) Andorra pediatrics. http://www.andorrapediatrics.com/ap_folders/hand-outs/knowledge/growth.htm
25. Tokuda J, Song S, Tuncali K, Tempany C, Hata N (2013) Configurable automatic detection and registration of fiducial frames for device to image registration in MRI guided prostate interventions. *Med Image Comput Comput Assist Interv* 16(03):355–362 [PubMed: 24505781]
26. Jussila J, Leppaniemi A, Paronen M, Kulomaki E (2005) Ballistic skin simulant. *Forensic Sci Int* 1(150):63–71

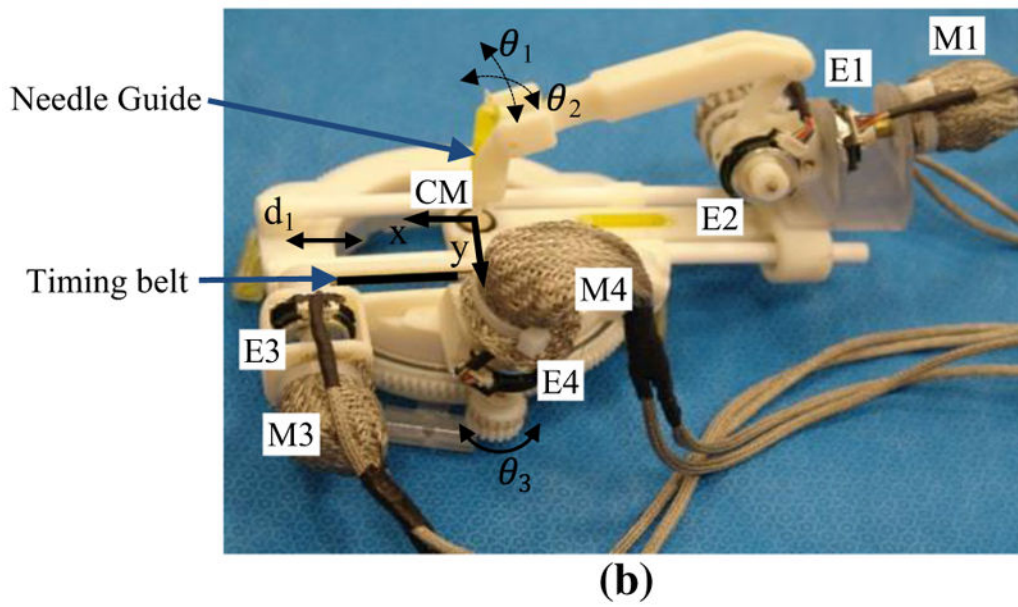
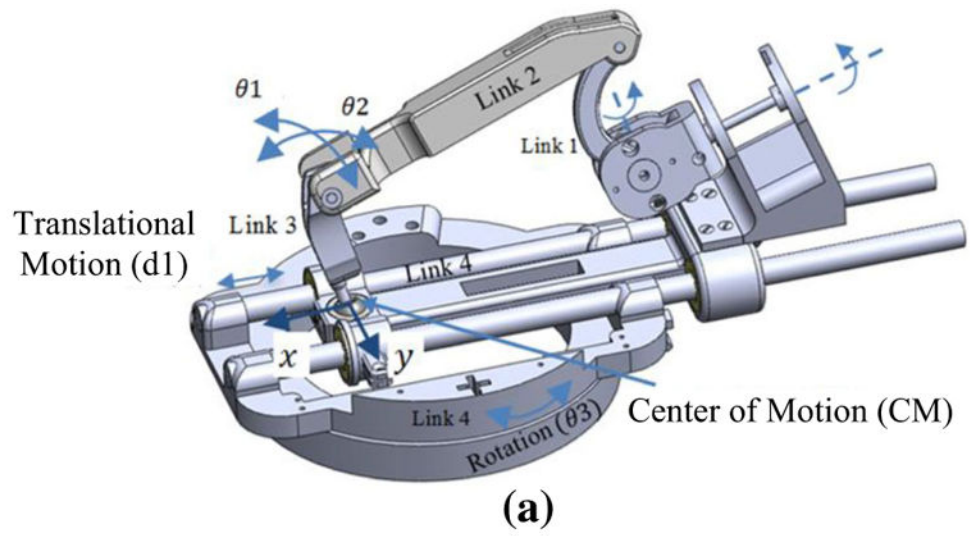


Fig. 1. Second prototype of the robot. **a** CAD model of main parts, **b** the robot with various parts labeled; *M* motors, *E* encoders

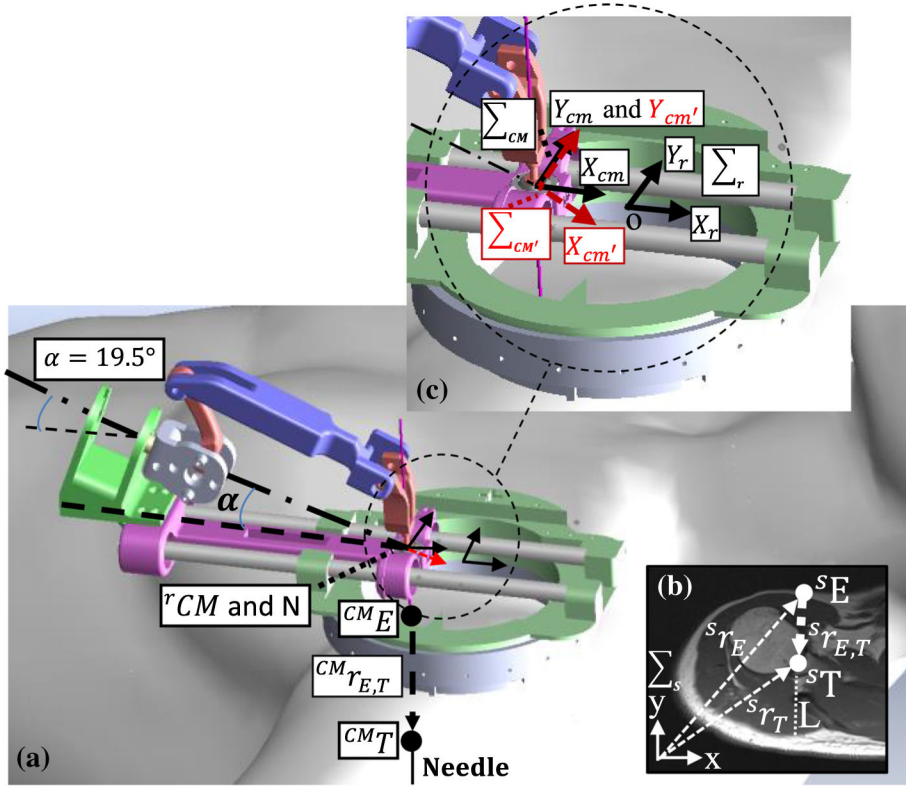


Fig. 2. Four coordinate frames are shown. Entry point and target point are shown as ${}^{CM}E$ and ${}^{CM}T$ in CM coordinate frame in (a) and as sE and sT in scanner coordinate frame in (b). ${}_r$ represents the robot coordinate frame that is attached and fixed to the center of the robot base; ${}_{cm}$ represents a coordinate frame that is attached to the CM and moves with CM. ${}_{cm'}$ represents a coordinate frame that is attached to the CM point and $X_{cm'}$ rotated 19.5° about Y_{cm} as shown in (c)

Author Manuscript

Author Manuscript

Author Manuscript

Author Manuscript

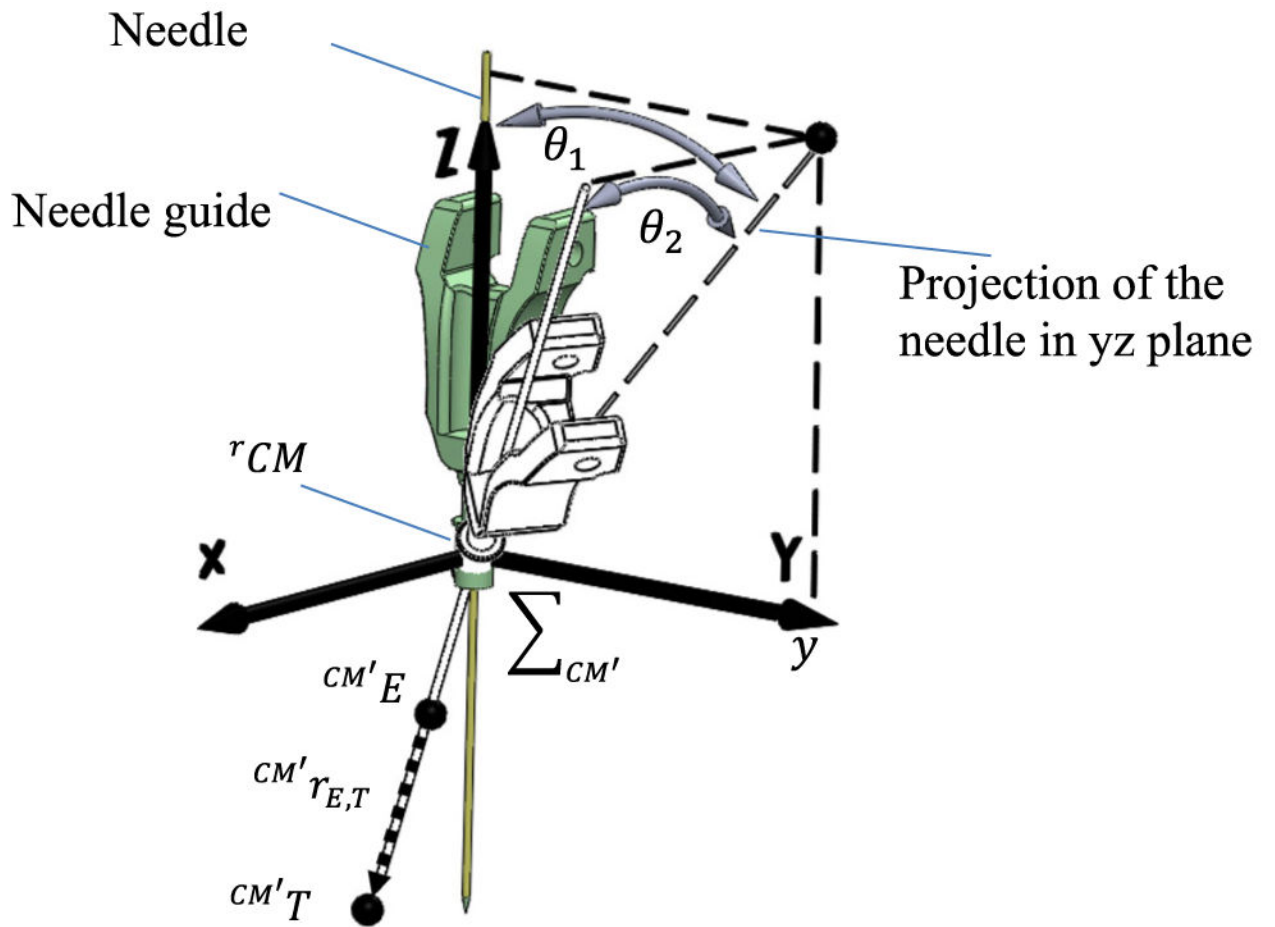


Fig. 3. Calculating rotation about x and y axes, i.e., γ and β

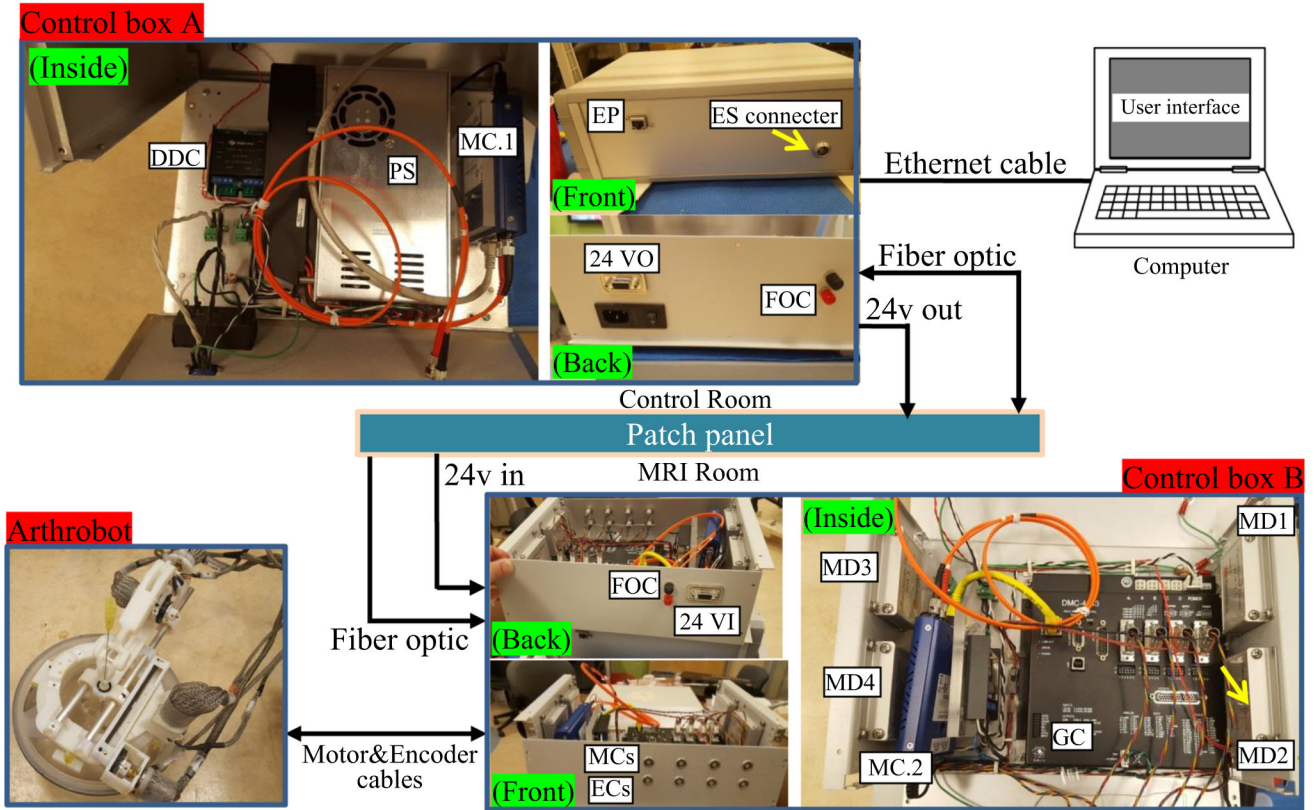


Fig. 4. Block diagram of the control system: control box A and computer are located in the control room, and control box B and robot are located in MRI room. Different components of the electronic system are labeled in this figure; *PS* power supply, *MC* media convertor, *GC* Galil controller, *MC* motor connector, *EC* encoder connector, *MD* motor driver, *ES* E-stop, *EP* Ethernet port, *DDC* DC-DC convertor, *FOC* fiber optic connector, *VI* volt input, *VO* volt output



Fig. 5. New proposed mounting method is shown. **a** Ring adaptor is embedded in a shoulder brace, **b** shoulder brace with embedded ring adaptor on a volunteer's shoulder

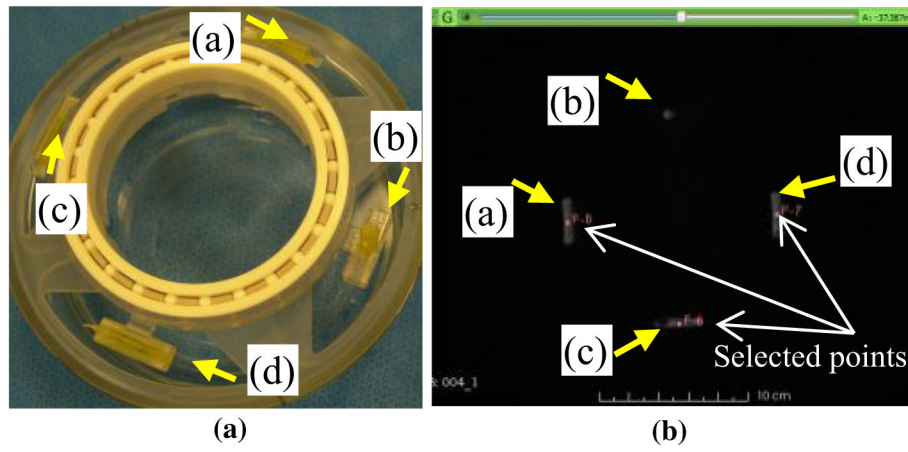


Fig. 6. Robot base with embedded tube fiducials for registration purposes, **a** location of the fiducials are shown, **b** fiducials are shown in the MRI images with manually selected approximate center points

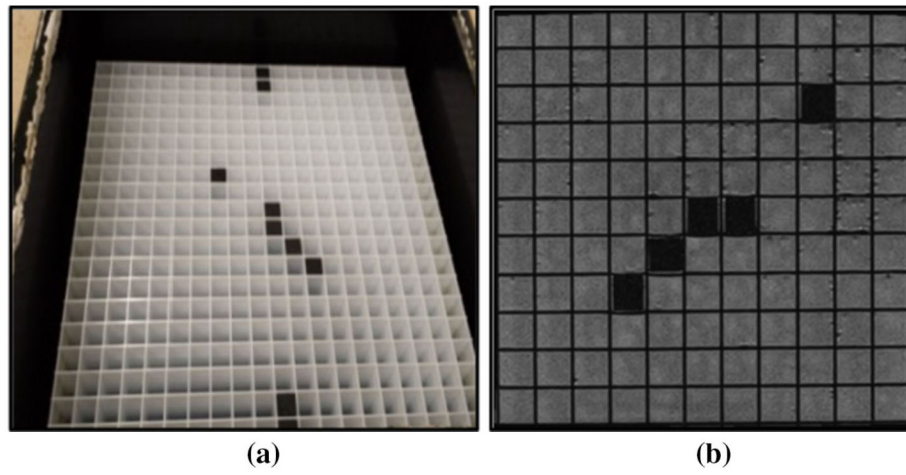


Fig. 7. Grating phantom with 1.5 cm by 1.5 cm cubes. **a** Photograph, **b** MRI image of part of the phantom

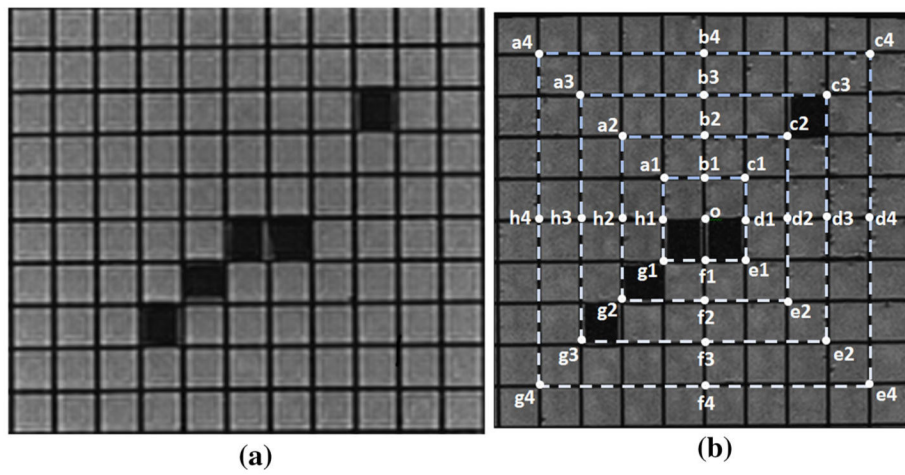


Fig. 8. MRI images of the grating phantom when the robot is placed on top. **a** MRI image shows insignificant distortion, **b** quantitative distortion study was performed in four zones, i.e., a1–h1, a2–h2, a3–h3, and a4–h4

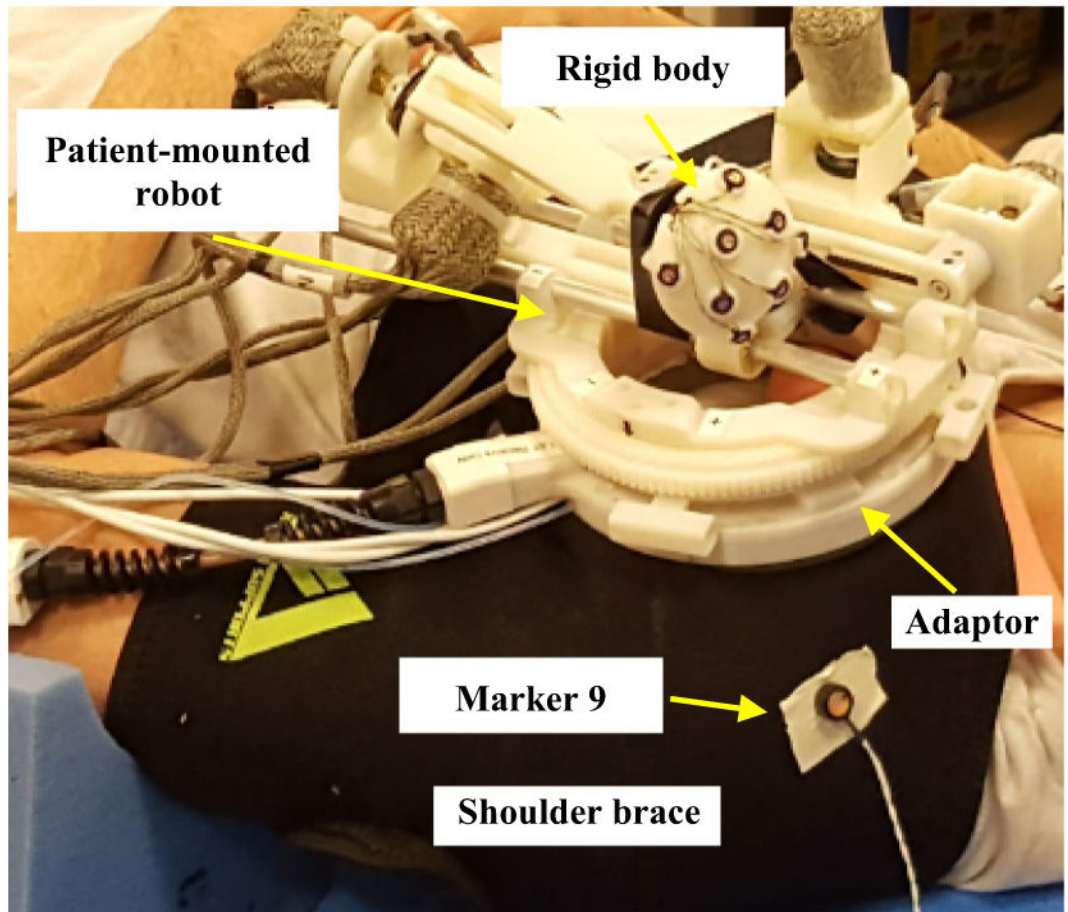


Fig. 9.
Setup for respiratory motion study. Shoulder is secured with shoulder brace, and rigid body was tracked by an optical tracker

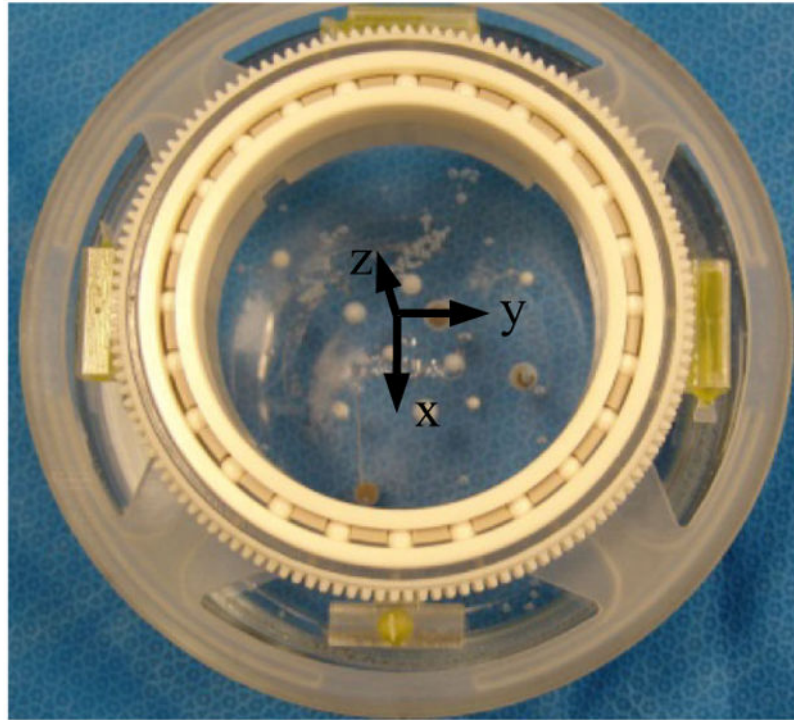


Fig. 10.
Four fiducials are used to estimate the robot coordinate system and origin with respect to image coordinate system

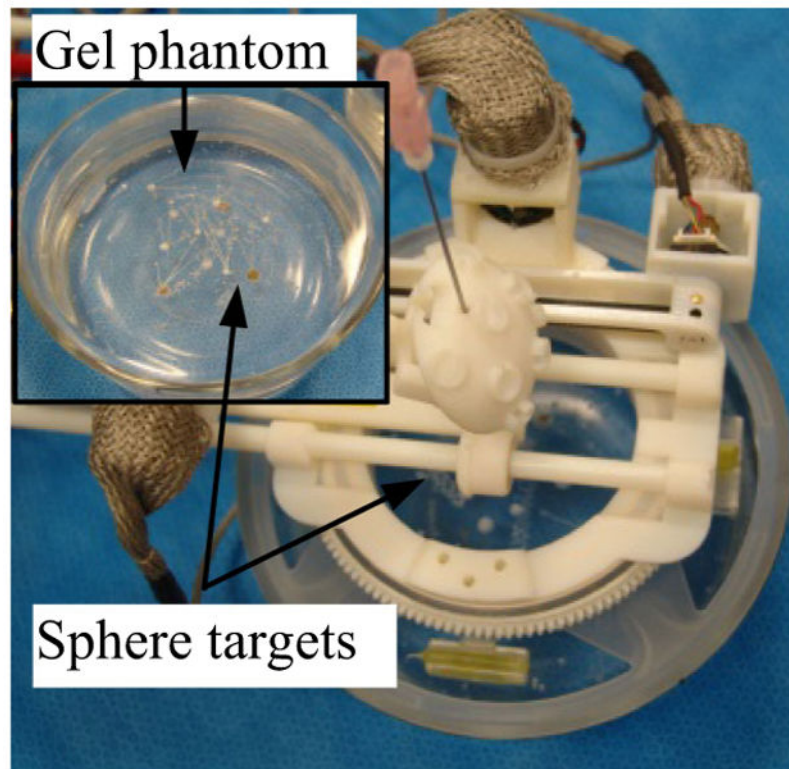


Fig. 11. Robot was placed on the gel phantom, and targets were reached using robot guidance

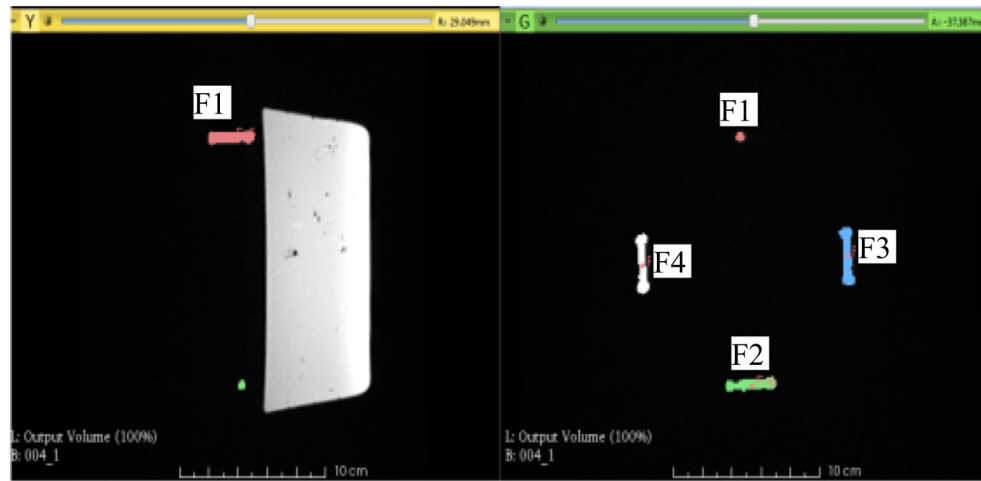


Fig. 12. MR image of gel phantom with registration tube fiducials after segmentation. Four fiducials, F1, F2, F3, and F4, are shown

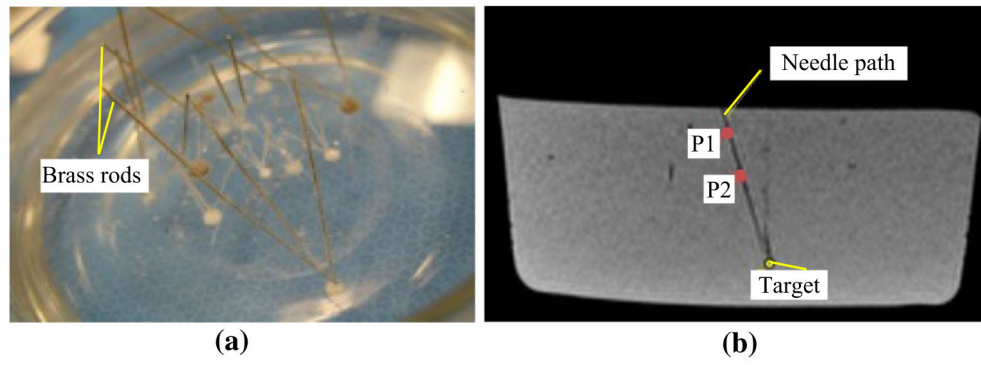


Fig. 13. Gel phantom after targeting 12 spheres from three different angles: **a** the gel phantom with brass rod placed into needle path, **b** MR image of the gel phantom showing one of the needle paths, target point, and selected points along the path

Table 1

Average and maximum distortion for each of the areas

Area	d%	Area2	d%	Area3	d%	Area4	d%
Ave.	0.83	Ave.	0.92	Ave.	0.56	Ave.	0.63
Max.	2.57	Max.	2.32	Max.	0.88	Max.	1.26

Table 2

Average and standard deviation of positional and rotational displacement of the rigid body attached to needle guide for 3 subjects

Subject	Error	Average	SD
Subject 1	Positional error relative to marker 9	0.9 mm	0.65 mm
	Angle	0.43°	0.4°
Subject 2	Positional error relative to marker 9	0.86 mm	0.64 mm
	Angle	0.35°	0.54°
Subject 3	Positional error relative to marker	0.76 mm	0.95 mm
	Angle	0.28°	0.48°
Total average	Displacement error	0.84 mm	0.74 mm
	Rotational error (degree)	0.34°	0.46°
	Rotational error (mm) (80 mm depth)	0.48 mm	0.64 mm
Combined error		1.32 mm	1.38 mm

Table 3

Targeting accuracy experimental results tested on a gel phantom

Set of targets	Average (mm)	Standard deviation (mm)
Targets on first layer	1.69	0.93
Targets on second layer	1.29	0.70
Targets on third layer	1.96	1.07
Total	1.64	0.90

Author Manuscript

Author Manuscript

Author Manuscript

Author Manuscript

Table 4

Estimated total error considering, (1) respiratory motion, (2) needle guide displacement during procedure, and (3) phantom study results

	Error source	Average (mm)	SD (mm)
1	Displacement of needle guide [18]	0.44	0.19
2	Related to respiratory motion	1.32	1.38
3	Phantom study	1.64	0.90
	Total	3.4	1.65

Author Manuscript

Author Manuscript

Author Manuscript

Author Manuscript